Harmonizing mechanical and thermal properties in Al/SiC superlattices: *Ab initio* machine-learning-potential study

Chol-Jun Yu,[1,*] Jong-Hyok Jang,[1] Kum-Chol Ri,[1] Song-Mu Kim,[2] Chol-Hyok Pak,[2] and Ryong-Jin Kim[2]

[1]*Chair of Computational Materials Design, Faculty of Materials Science, Kim Il Sung University, Ryongnam-Dong, PO Box 76, Taesong District, Pyongyang, DPR Korea*

[2]*Institute of Nanomaterials, Faculty of Materials Science, Kim Il Sung University, Ryongnam-Dong, PO Box 76, Taesong District, Pyongyang, DPR Korea*

(Received 11 August 2023; revised 24 October 2023; accepted 2 January 2024; published 22 February 2024)

The aluminum matrix composites (AMCs) reinforced with silicon carbide have attracted significant interest in several high-tech industries. In this work, we provide an insightful atomistic understanding of harmonizing mechanical and thermal properties of Al/SiC composites using superlattice models and *ab initio* machine-learning-potential calculations. Our calculations reveal the optimal value of SiC percentage as 25% ∼ 27% in superlattice-type composites for combining high mechanical strength with ductility. With increasing the SiC percentage, the coefficients of thermal expansion decrease in the range of 0.5–2.5 × 10^{-5} K^{-1}, while the lattice thermal conductivity increases in the range of 24–38 W m^{-1} K^{-1} at 300 K. These data will help tailor AMCs to the terms desired with the proposed *ab initio* based computational procedure.

DOI: 10.1103/PhysRevB.109.075426

I. INTRODUCTION

Nanocomposites have attracted significant research interest for effectively tuning their mechanical and thermal properties. Typically, aluminum matrix composites (AMCs) reinforced with nanophase ceramics like silicon carbide whisker (SiCw) [1] combined high strength with ductility and low thermal expansion with high thermal conductivity [2–4]. With this, well-designed AMCs became indispensable requisites for several high-tech industries, such as aerospace, automobile, and electronic fields [5]. According to the terms desired, optimal properties of SiCw-reinforced AMCs are mainly obtained by manipulating the size and distribution of SiCw. In particular, the optimal value of SiCw volume fraction is a critical factor in achieving high-performance of AMCs, but is not easy to determine when based on experiment only.

Meanwhile, because the load and heat are transferred through the interface, Al/SiCw interface plays a decisive part in improving the properties [6]. Here, the atomistic structure of the interface is the key issue, together with how to improve the wettability and adhesion of Al/SiCw interface. To address the issue, advanced materials modeling and simulation techniques have been applied, including *ab initio* density functional theory (DFT) [7–9] and classical molecular dynamics (CMD) [10]. However, most of the previous DFT works adopted the slab models to study bonding and electronic nature of the interface, thereby being limited in quantitative prediction of bulk properties such as elastic constants and coefficients of thermal expansion. On the other hand, variation tendency of such properties could not be explored by CMD, which moreover has an intrinsic limit in accuracy due to the use of empirical interatomic potential.

In this work, we adopt the superlattice (SL) models to investigate the mechanical and thermal properties of Al/SiCw nanocomposites. In fact, phonons and related thermal transport in SLs have long been challenging issues in physical and chemical sciences [11–14], with different forms such as semiconductor/semiconductor [15–17], semiconductor/metal [18–20], and amorphous/crystal [21] SLs. In this regard, we compute not only elastic constants but also phonons, thermal expansion coefficients, and lattice thermal conductivities of Al/SiCw SLs as varying the SiC atomic percentage in SLs.

II. METHOD

To construct the superlattices, the interface is composed of fcc-Al(110) (4 × 1) surface supercell and 6H-SiC(110) or (11=20) surface unit cell, and the number of Al atomic layers varies from 5 to 11 with an interval of 2 while fixing the number of SiC atomic layers as 3. Hereafter, the superlattice models are denoted as Aln/SiC3 with $n = 5, 7, 9, 11$ (see Figs. S1 and S2 in the Supplemental Material [22]).

For calculations, we applied DFT method combined with classical molecular mechanics (CMM) using *ab initio* MD-derived machine-learning interatomic potential (MLIP). The structural optimizations of single crystals and superlattices were performed using the pseudopotential plane-wave method, as implemented in the QUANTUM ESPRESSO (QE, version 7.0) package [23]. The stress-strain method was used to calculate the elastic constants, as implemented in the ELASTIC code [24] in connection with QE. We used the ultrasoft pseudopotentials for the ion-electron interaction, as provided in the GBRV library [25], and the Perdew-Burke-Ernzerhof (PBE)

*cj.yu@ryongnamsan.edu.kp

functional [26] for the exchange-correlation interaction. For CMM calculations, we built MLIP [27–31] by training over short *ab initio* MD trajectories and using the moment tensor potential form [32,33]. Phonons and coefficients of thermal expansion were calculated within the quasiharmonic approximation (QHA) using the ALAMODE code [34,35] in connection with QE and LAMMPS [36]. Computational details was provided in the Supplemental Material [22] (see also Refs. [37–44] therein).

III. RESULT AND DISCUSSION

To start with we performed structural optimizations of the unit cells of the 6H-SiC (space group $P6_3mc$), fcc-Al ($Fm = 3m$) crystals, and Aln/SiC3 SLs (see Table S1 in the Supplemental Material [22]). For the 6H-SiC unit cell, the optimized lattice constants are $a = 3.094$ and $c = 15.183$ Å with relative errors of 0.43% and 0.38% compared with the experimental values of 3.081 and 15.125 Å [45]. The optimized lattice constant of fcc-Al unit cell is $a = 4.047$ Å with a relative error of -0.07% in comparison with the experimental value of 4.050 Å [46]. When constructing the superlattices from fcc-Al(110) and 6H-SiC(110) surfaces with these calculated lattice constants, the lattice mismatches are 6.2% and 6.4% in the a (15.685 Å) and b (5.541 Å) directions, respectively. These mismatches are smaller than 7.6% in the case of Al(111)/6H-SiC(0001) interface [7,8], indicating that the present selection of surface indices for interface is more reasonable. With variable cell relaxations using QE, the SL unit cells were found to be negligibly deviated from the original orthorhombic structure (space group $Pmc21$), which was therefore kept in further calculations.

Then, we estimated the formability of the superlattices from their constituent bulks and the binding strength between the contacting interface layers. To this end, we calculated the formation and binding energies per atom as increasing the Al layers (conversely decreasing the SiC percentage). The formation energy is 1.10 eV for Al5/SiC3 SL and decreases as increasing the Al atomic layers to 0.59 eV for Al11/SiC3 SL (see Table S2 in the Supplemental Material [22]). The positive values indicate that formation of the superlattices from the constituent bulks is an endothermic process. We find the formation energy as a linear function of SiC atomic percentage like $E_f(x) = 2.75x - 0.21$ (eV), where $x = n_{\mathrm{SiC}}/n_{\mathrm{tot}}$ with the number of SiC atoms n_{SiC} and the total number of atoms n_{tot}, as shown in Fig. 1(c). Therefore, the SL formability can increase as decreasing the SiC portion in AMCs, and even the formation can be exothermic below $p_{\mathrm{SiC}} \approx 7.6\%$ according to the formula. In contrast with this trend, the binding strength was found to decrease as decreasing the SiC percentage since the binding energy per atom was described by a linear function of x, $E_b(x) = -0.7186x + 0.0016$ (eV). From this equation, the negative binding energy is obtained for the almost whole range of $x \in (0, 1)$, indicating an attractive binding between the Al and SiC layers. Such strong binding is supported from the newly formed Al-C (2.03 Å) and Al-Si (2.46 Å) covalent bonds at the interface. This is caused by charge redistribution upon the interface formation, as depicted in Fig. 1(d) (see Fig. S3 in the Supplemental Material [22]), where a considerable amount of accumulated charge is observed at the middle space between the Al and SiC layers.

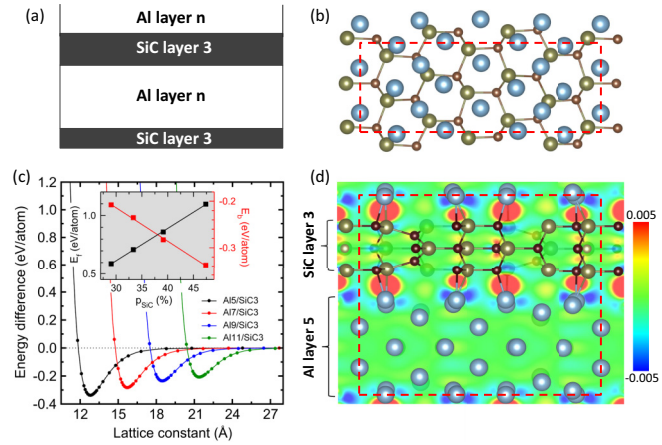

FIG. 1. (a) Sketch of Aln/SiC3 superlattice structures. (b) Top and (d) side views of Al5/SiC3 superlattice with isosurface plot of electron density difference, where positive (negative) value means electron gain (loss). Blue, green, and brown balls denote Al, Si, and C atoms, respectively. Red-colored dashed lines indicate the superlattice unit cell. (c) Energy difference of superlattices as increasing the distance between Al and SiC layers in the c direction (i.e., lattice constant c). Inset shows the superlattice formation energy per atom E_f (black) and the interface binding energy per atom E_b (red) as functions of SiC atom percentage (p_{SiC}).

Next, we consider the mechanical properties of the Aln/SiC3 superlattices by calculating the elastic constant tensor C_{ij} and the derived properties, which play an important part in describing their mechanical strengths. Figure 2 presents the calculated elastic constants based on the stress-

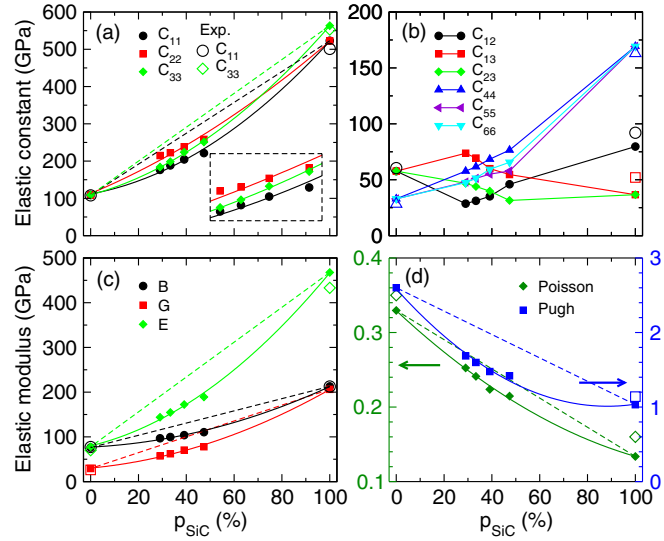

FIG. 2. Mechanical properties of Al/SiC superlattices as varying the SiC atomic percentage (p_{SiC}). (a) Principal and (b) shear components of elastic stiffness constant tensor, (c) bulk (B), shear (G) and Young's (E) moduli, and (d) Poisson's and Pugh's ratios. Solid lines represent quadratic regression and dashed lines show linear relation. Empty symbols indicate experimental values.

strain approach, elastic moduli, and Poisson's and Pugh's ratios as functions of SiC percentage (see Tables S3–S5 and Fig. S4 in the Supplemental Material [22]). At a glance, those quantities show gradual variation tendencies without a big anomaly as going from Al to SiC through Aln/SiC3 SLs, except the shear components (C_{12}, C_{13}, C_{23}) of elastic constant tensor [Fig. 2(b)].

The principal elastic constants (C_{ii}, $i = 1, 2, 3$) in superlattices were found to gradually increase with increasing the SiC atomic percentage as shown in Fig. 2(a). For the fcc-Al bulk, C_{11} is 109.0 GPa in good agreement with the experimental value of 106.8 GPa [46]. This is much smaller than both $C_{11} = 523$ and $C_{33} = 563$ GPa for the 6H-SiC crystal (comparable with the experimental values of 500 and 564 GPa [37]), verifying that Al metal used as a matrix is mechanically much weaker than SiC ceramics used as a reinforcing agent. Our calculations reveal that the principal elastic constants look like following the quadratic functions of x (solid lines) rather than linear function (dashed lines), like $C_{11}(x) = 111.85 + 116.45x + 293.52x^2$ (GPa), $C_{22}(x) = 113.13 + 267.78x + 140.52x^2$ (GPa), and $C_{33}(x) = 109.41 + 174.25x + 279.42x^2$ (GPa). Such quadratic variation tendencies are also observed in elastic moduli, which act as a mechanical strength check of a polycrystalline solid, including bulk (B), shear (G), and Young's modulus (E) [Fig. 2(c)]. The quadratic regression to the calculated values gives the functions $B(x) = 77.18 + 26.27x + 108.93x^2$ (GPa), $G(x) = 30.28 + 49.91x + 125.69x^2$ (GPa), and $E(x) = 80.08 + 127.71x + 258.97x^2$ (GPa). From these analyses, it becomes clear that the mechanical strength of Al/SiC composites is enhanced as increasing the SiC percentage, following the quadratic tendency. Such enhancement of mechanical strength is mostly ascribed to three factors: (i) better elastic performance of SiC than pure Al, (ii) increasing the Al-SiC interface binding strength as increasing the SiC content as stated above, and (iii) mismatch of the coefficient of thermal expansion (CTE) between SiC and Al as will be discussed below. The better interfacial bonding induces more effective load transfer between the matrix and reinforcement [10] while the CTE mismatch creates the dislocations in the near-interface areas [47].

To determine the critical value of SiC percentage at which the composite is converted from ductile to brittle, we derived the Poisson's ratio (ν) and Pugh's ratio (μ). As shown in Fig. 2(d), these ratios decrease from $\nu = 0.33$ and $\mu = 2.60$ for fcc-Al (experimental value $\nu = 0.35$ [48]) to $\nu = 0.13$ and $\mu = 1.03$ for 6H-SiC, along the quadratic functions of $\nu(x) = 0.33 - 0.30x + 0.10x^2$ and $\mu(x) = 2.58 - 3.56x + 2.02x^2$. According to the criteria for ductility ($\nu \geqslant 0.26$ or $\mu \geqslant 1.75$), the critical x values are determined to be $x_\nu = 0.25$ and $x_\mu = 0.28$.

To proceed, we investigate the electron conductance across the interface and along the layers by calculating electronic local density of states (LDOS). Figure 3(a) shows the calculated LDOS in Al5/SiC3 SL as a typical example. A band gap of ~3.5 eV is found in the SiC layers while no gap in the Al layers, indicating that the electron transfer is not allowed along the SiC layer but allowed along the Al layers. At the interface, however, we find a relatively high potential barrier, which inhibits the electron transfer through the Al-SiC contact. This indicates that the thermal conductivity of the composite cannot be dominated by electrons but phonons.

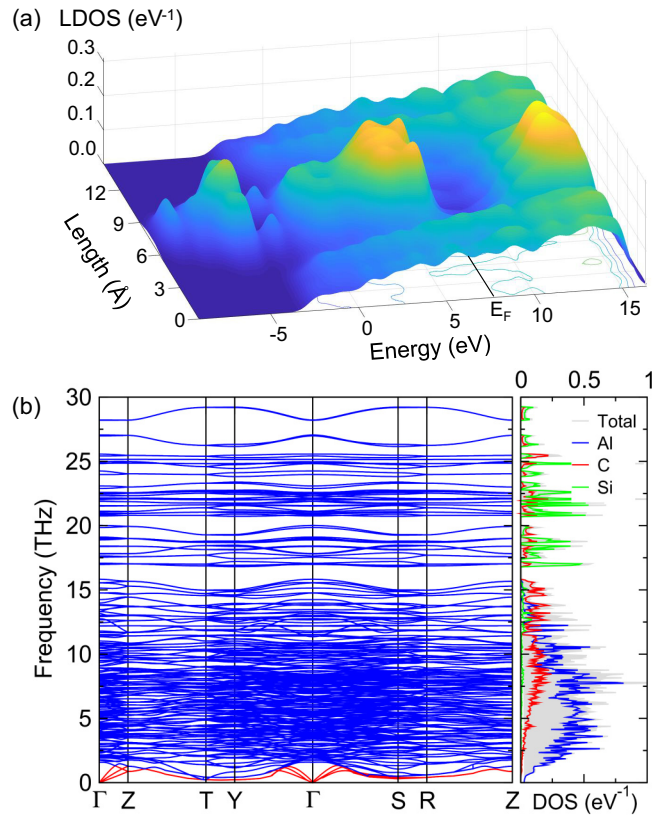

FIG. 3. (a) Electronic local density of states (LDOS) along the z axis (longitudinal axis), where the Fermi energy E_F is marked, and (b) phonon dispersion curves along the high-symmetry points of Brillouin zone, where red (blue) lines indicate the acoustic (optic) modes, with phonon density of states (DOS) with atomic contributions in Al5/SiC3 superlattice.

Consecutively, we investigate the thermal properties including CTEs (α) and lattice thermal conductivities (κ_L) as functions of temperature. At this step of calculation, we rely on the CMM using *ab initio* MD-derived MLIP for the SLs, which provide a DFT level accuracy with a very low computational cost [32,33]. The phonon dispersions were calculated at each value of volume using LAMMPS with MLIP constructed in this work to obtain the vibrational free energy $F^{\text{vib}}(T, V)$, thus the Helmholtz free energy $F(T, V) = E(V) + F^{\text{vib}}(T, V)$.

Figure 3(b) shows the phonon dispersion and phonon density of states (DOS) in Al5/SiC3 SL as a typical example calculated at the equilibrium volume. Note that those of fcc-Al and 6H-SiC bulk were also calculated and agreed well with the available experiment, and those of other superlattices show similar features to Al5/SiC3 SL (see Figs. S8 and S9 in the Supplemental Material [22]). No anharmonic phonon modes with imaginary frequency were observed in dispersions, indicating that the superlattice crystals are thermodynamically stable. From the phonon DOS, it is revealed that the Al atoms dominate the acoustic and low-frequency optical modes below 13 THz, while the higher-frequency optical modes are dominated by the Si and C atoms. This indicates that the lattice

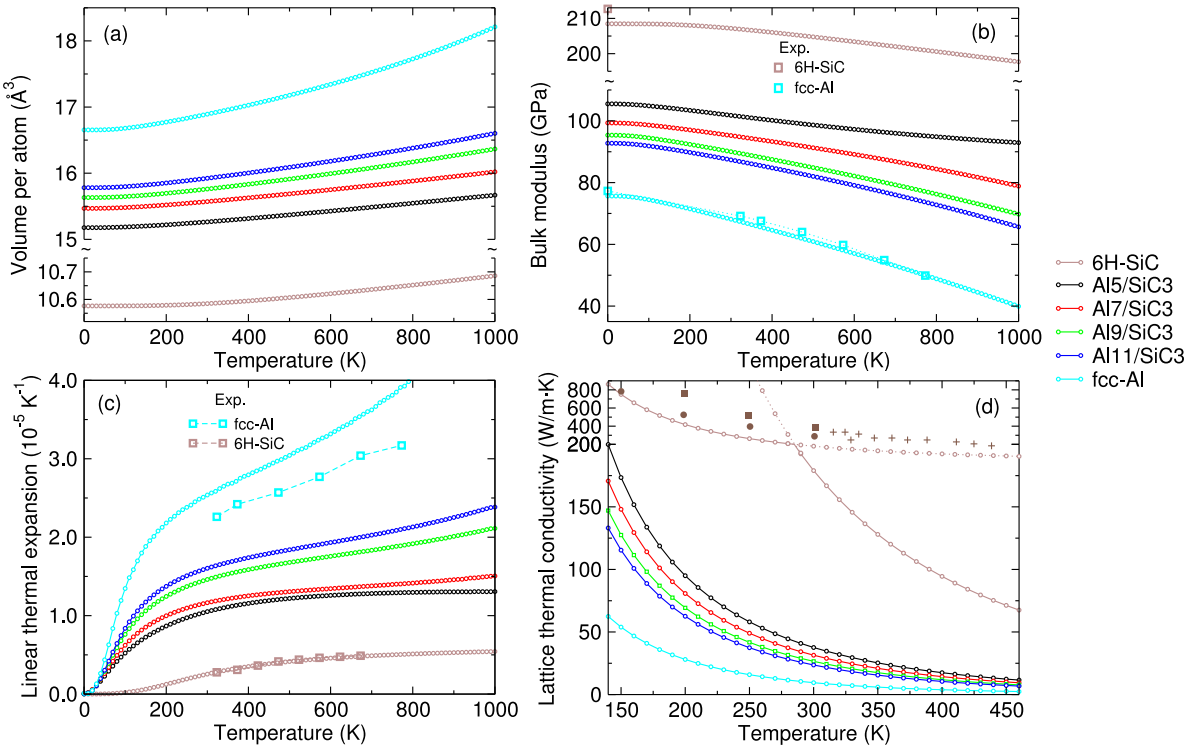

FIG. 4. Thermal properties as functions of temperature in fcc-Al, 6H-SiC, and their composite superlattices Aln/SiC3 ($n = 5, 7, 9, 11$). (a) Equilibrium unit-cell volume per atom, (b) bulk modulus, (c) coefficients of linear thermal expansion, where the experimental values are provided for fcc-Al at 300 K [46,49] and for 6H-SiC [50], and (d) lattice thermal conductivities, where the experimental values for 6H-SiC are provided [51–53].

thermal conductance in Al/SiC composite is dominated by Al atoms with small contribution from SiC part. As increasing the Al layers, the contribution from SiC to acoustic mode is found to gradually decrease.

In Fig. 4(a), we show the equilibrium unit-cell volume per atom as a function of temperature determined by fitting the F-V data to the EOS. For all the crystalline solids, the volumes increase rightly as increasing temperature. At each temperature, the unit-cell volume per atom increases as decreasing the SiC percentage in the composites. This is related with that the mass density of 6H-SiC (3.17 g cm^{-3}) is higher than that of fcc-Al (2.70 g cm^{-3}). Note that the mass densities of SLs range from 2.62 ($n = 5$) to 2.66 g cm^{-3} ($n = 11$), being lower than those of parent bulks possibly due to the interfacial space. By contrast, the bulk modulus decreases as increasing temperature naturally for all the crystals, and as decreasing the SiC percentage in composites at every temperature [see Fig. 4(b)].

Using the calculated $V(T)$ data, we derived the linear CTE of $\beta(T) = \frac{1}{3V}(\partial V/\partial T)_P$. As shown in Fig. 4(c), 6H-SiC bulk has much lower CTE than fcc-Al, for which the calculated β value at 300 K is 2.54×10^{-5} K^{-1} close to the experimental value of 2.31×10^{-5} K^{-1} [46]. Therefore, $\beta(T)$ decreases with an increase of SiC percentage in composites at every temperature, ranging from 0.5×10^{-5} K^{-1} of 6H-SiC to 2.5×10^{-5} K^{-1} of fcc-Al. That is, Al/SiC composites can exhibit lower CTE than Al metal due to the existence of SiC that has very low CTEs (see Figs. S12 and S13 in the Supplemental Material [22]). It is worth noting that the big thermal mismatch between SiC and Al induces dislocations around the interface during the cooling process of the composite fabrication, strengthening the small punched zone near the interface.

Finally, we estimate the lattice thermal conductivities (κ_L) using the calculated elasticity-derived quantities with the Cahill's model [54]. Giving the theoretical minimum of κ_L, this model is expressed by $\kappa_L^{\min}(T) = (\frac{\pi}{6})^{1/3} k_B n_a^{2/3} \sum_{i=1}^{3} \upsilon_i (\frac{\theta_i}{T})^2 \int_0^{\theta_i/T} \frac{x^3 e^x}{(e^x-1)^2} dx$, where n_a is the the number of atoms per unit volume, $\upsilon_{1,2} = \upsilon_l$ and $\upsilon_3 = \upsilon_t$ are the elastic wave velocities in longitudinal and transverse acoustic phonon modes, and θ_i is the corresponding Debye temperature (see Table S6 in the Supplemental Material [22]). As shown in Fig. 4(d), the calculated κ_L for 6H-SiC was slightly underestimated compared with the experiments [51–53] and much higher than that of fcc-Al. The Aln/SiC3 SLs exhibit reasonably high κ_L, e.g., ranging from 24 to 38 W m^{-1} K^{-1} at 300 K, and show an increasing tendency with increasing the SiC percentage. This is associated with that SiC has higher acoustic wave velocities and higher Debye temperature than Al and the heat-carrying low-energy phonon modes of the composite are dominated by Al atoms.

In conclusion, we have investigated the mechanical and thermal properties of the Al/SiC superlattices using the DFT and CMM calculations with *ab initio* derived MLIP. Our calculations revealed the optimal value of SiC percentage for high mechanical strength with keeping ductility, and the

reasonably low CTE with high lattice thermal conductivities. This work highlights the atomistic insights into harmonizing mechanical and thermal properties of Al/SiC composites.

ACKNOWLEDGMENT

The work is supported by the State Commission of Science and Technology (Grant No. 2021-12), DPR Korea.

[1] R. Madar, Materials science: Silicon carbide in contention, Nature (London) **430**, 974 (2004).

[2] J. Osterman, A. Hallén, and S. Anand, Carrier profiling of Al-doped 4H-SiC by scanning spreading resistance microscopy, Appl. Phys. Lett. **81**, 3004 (2002).

[3] A. Frazzetto, F. Giannazzo, P. Fiorenza, V. Raineri, and F. Roccaforte, Limiting mechanism of inversion channel mobility in Al-implanted lateral 4H-SiC metal-oxide semiconductor field-effect transistors, Appl. Phys. Lett. **99**, 072117 (2011).

[4] J. Huang, Z. Wang, J. Gan, Y. Yang, G. Wu, and Q. Meng, Investigation of fatigue performance improvement in SiCw/Al composites with different modified shot peening treatments by considering surface mechanical properties, J. Alloys Compd. **728**, 169 (2017).

[5] N. Li and X. Y. Liu, Review: Mechanical behavior of metal/ceramic interfaces in nano layered composites-experiments and modeling, J. Mater. Sci. **53**, 5562 (2018).

[6] W. Wunderlich, The atomistic structure of metal/ceramic interfaces is the key issue for developing better properties, Metals **4**, 410 (2014).

[7] C. Wang, W. Chen, and J. Xie, Effects of transition element additions on the interfacial interaction and electronic structure of Al(111)/6H-SiC(0001) interface: A first-principles study, Materials **14**, 630 (2021).

[8] Q. Wu, J. Xie, A. Wang, C. Wang, and A. Mao, Effects of vacancies at Al(111)/6H-SiC(0001) interfaces on deformation behavior: A first-principle study, Comput. Mater. Sci. **158**, 110 (2019).

[9] C. Wang, W. Chen, Y. Jia, and J. Xie, Calculating study on properties of Al (111)/6H-SiC (0001) interfaces, Metals **10**, 1197 (2020).

[10] J. M. Zhan, W. R. Jian, X. C. Tang, Y. L. Han, W. H. Li, X. H. Yao, and L. Y. Meng, Tensile deformation of nanocrystalline Al-matrix composites: Effects of the sic particle and graphene, Comput. Mater. Sci. **156**, 187 (2019).

[11] C. Dansou, C. Paillard, and L. Bellaiche, Controlling the properties of $PbTiO_3/SrTiO_3$ superlattices by photoexited carriers, Phys. Rev. B **106**, L220101 (2022).

[12] M. N. Luckyanova, J. Garg, K. Esfarjani, A. Jandl, M. T. Bulsara, A. J. Schmidt, A. J. Minnich, S. Chen, M. S. Dresselhaus, Z. Ren *et al.*, Coherent phonon heat conduction in superlattices, Science **338**, 936 (2012).

[13] T. Juntunen, O. Väänskä, and I. Tittonen, Anderson localization quenches thermal transport in aperiodic superlattices, Phys. Rev. Lett. **122**, 105901 (2019).

[14] D. N. Talwar, S. Semone, and P. Becla, Interface-induced localization of phonons in BeSe/ZnSe superlattices, Appl. Phys. Lett. **117**, 183104 (2020).

[15] D. N. Talwar, Atypical phonon modes in zinc-blende BN/GaN superlattices, Appl. Phys. Lett. **102**, 252101 (2013).

[16] P. Chen, N. A. Katcho, J. P. Feser, W. Li, M. Glaser, O. G. Schmidt, D. G. Cahill, N. Mingo, and A. Rastelli, Role of surface-segregation-driven intermixing on the thermal transport through planar Si/Ge superlattices, Phys. Rev. Lett. **111**, 115901 (2013).

[17] L. F. Llin, A. Samarelli, S. Cecchi, T. Etzelstorfer, E. M. Gubler, D. Chrastina, G. Isella, J. Stangl, J. M. R. Weaver, P. S. Dobson *et al.*, The cross-plane thermoelectric properties of p-Ge/$Si_{0.5}Ge_{0.5}$ superlattices, Appl. Phys. Lett. **103**, 143507 (2013).

[18] S. Chakraborty, H. Uchiyama, M. Garbrecht, V. Bhatia, A. I. K. Pillai, J. P. Feser, D. T. Adroja, S. Langridge, and B. Saha, Phononic bandgap and phonon anomalies in HfN and HfN/ScN metal/semiconductor superlattices measured with inelastic x-ray scattering, Appl. Phys. Lett. **117**, 111901 (2020).

[19] B. Saha, Y. R. Koh, J. P. Feser, S. Sadasivam, T. S. Fisher, A. Shakouri, and T. D. Sands, Phonon wave effects in the thermal transport of epitaxial TiN/(Al,Sc)N metal/semiconductor superlattices, J. Appl. Phys. **121**, 015109 (2017).

[20] J. D. Emery, B. Detlefs, H. J. Karmel, L. O. Nyakiti, D. K. Gaskill, M. C. Hersam, J. Zegenhagen, and M. J. Bedzyk, Chemically resolved interface structure of epitaxial graphene on SiC(0001), Phys. Rev. Lett. **111**, 215501 (2013).

[21] R. Anufriev, S. Tachikawa, S. Gluchko, Y. Nakayama, T. Kawamura, L. Jalabert, and M. Nomura, Cross-plane thermal conductivity in amorphous Si/SiO_2 superlattices, Appl. Phys. Lett. **117**, 093103 (2020).

[22] See Supplemental Material at http://link.aps.org/supplemental/10.1103/PhysRevB.109.075426 for computational details, tables for optimized lattice parameters, interface formation energies, elastic constants, elastic moduli and derived elastic and thermal properties, and figures for structural modeling of superlattices, electron density difference in superlattices, stress-strain curves, energy-volume curves, phonon dispersions, Helmholtz free energy vs volume curves, heat capacity, linear thermal expansion coefficients, and lattice thermal conductivities.

[23] P. Giannozzi, S. Baroni, N. Bonini, M. Calandra, R. Car, C. Cavazzoni, D. Ceresoli, G. L. Chiarotti, M. Cococcioni, I. Dabo *et al.*, QUANTUM ESPRESSO: a modular and open-source software project for quantum simulations of materials, J. Phys.: Condens. Matter **21**, 395502 (2009).

[24] R. Golesorkhtabar, P. Pavone, J. Spitaler, P. Puschnig, and C. Draxl, ElaStic: a tool for calculating second-order elastic constants from first principles, Comput. Phys. Commun. **184**, 1861 (2013).

[25] K. F. Garrity, J. W. Bennet, K. M. Rabe, and D. Vanderbilt, Pseudopotentials for high-throughput DFT calculations, Comput. Mater. Sci. **81**, 446 (2014).

[26] J. P. Perdew, K. Burke, and M. Ernzerhof, Generalized gradient approximation made simple, Phys. Rev. Lett. **77**, 3865 (1996).

[27] J. T. Williman, K. Nguyen-Cong, A. S. Williams, A. B. Belonochko, S. G. Moore, A. P. Thompson, M. A. Wood, and I. I. Olaynik, Machine learning interatomic potential for simula-

tion of carbon at extreme condition, Phys. Rev. B **106**, L180101 (2022).
[28] X. Ouyang, W. Chen, Y. Zhang, F. Zhang, Y. Zhuang, X. Jie, L. Liu, and D. Wang, Structural phase transition involving octahedron tilting and ion migration in metal-halide perovskites: A machine-learning study, Phys. Rev. B **108**, L020103 (2023).
[29] K. T. Butler, D. W. Davies, H. Cartwright, O. Isayev, and A. Walsh, Machine learning for molecular and materials science, Nature (London) **559**, 547 (2018).
[30] G. Sivaraman, J. Guo, L. Ward, N. Hoyt, M. Williamson, I. Foster, C. Benmore, and N. Jackson, Automated development of molten salt machine learning potentials: Application to LiCl, J. Phys. Chem. Lett. **12**, 4278 (2021).
[31] R. Jinnouchi, K. Miwa, F. Karsai, G. Kresse, and R. Asahi, On-the-fly active learning of interatomic potentials for large-scale atomistic simulations, J. Phys. Chem. Lett. **11**, 6946 (2020).
[32] E. V. Podryabinkin, E. V. Tikhonov, A. V. Shapeev, and A. R. Oganov, Accelerating crystal structure prediction by machine-learning interatomic potentials with active learning, Phys. Rev. B **99**, 064114 (2019).
[33] P. Korotaev, I. Novoselov, A. Yanilkin, and A. Shapeev, Accessing thermal conductivity of complex compounds by machine learning interatomic potentials, Phys. Rev. B **100**, 144308 (2019).
[34] T. Tadano and S. Tsuneyuki, Self-consistent phonon calculations of lattice dynamical properties in cubic $SrTiO_3$ with first-principles anharmonic force constants, Phys. Rev. B **92**, 054301 (2015).
[35] T. Tadano and S. Tsuneyuki, Quartic anharmonicity of rattlers and its effect on lattice thermal conductivity of clathrates from first principles, Phys. Rev. Lett. **120**, 105901 (2018).
[36] S. Plimpton, Fast parallel algorithms for short-range molecular dynamics, J. Comput. Phys. **117**, 1 (1995).
[37] R. Thokala and J. Chaudhuri, Calculated elastic constants of wide band gap semiconductor thin films with a hexagonal crystal structure for stress problems, Thin Solid Films **266**, 189 (1995).
[38] W.-W. Xu, F. Xia, L. Chen, M. Wu, T. Gang, and Y. Huang, High-temperature mechanical and thermodynamic properties of silicon carbide polytypes, J. Alloys Compd. **768**, 722 (2018).
[39] H. Xie, S. Hao, J. Bao, T. J. Slade, G. J. Snyder, C. Wolverton, and M. G. Kanatzidis, All-inorganic halide perovskites as potential thermoelectric materials: Dynamic cation off-centering induces ultralow thermal conductivity, J. Am. Chem. Soc. **142**, 9553 (2020).
[40] W. Xie, J. He, H. J. Kang, X. Tang, S. Zhu, M. Laver, S. Wang, J. R. Copley, C. M. Brown, Q. Zhang *et al.*, Identifying the specific nanostructures responsible for the high thermoelectric performance of $(Bi,Sb)_2Te_3$ nanocomposites, Nano Lett. **10**, 3283 (2010).
[41] E. V. Podryabinkin and A. V. Shapeev, Active learning of linearly parametrized interatomic potentials, Comput. Mater. Sci. **140**, 171 (2017).
[42] G. Kresse and J. Furthmüller, Effciency of ab-initio total energy calculations for metals and semiconductors using a plane-wave basis set, Comput. Mater. Sci. **6**, 15 (1996).
[43] G. Kresse and J. Furthmüller, Efficient iterative schemes for ab initio total-energy calculations using a plane-wave basis set, Phys. Rev. B **54**, 11169 (1996).
[44] A. V. Shapeev, Moment tensor potentials: A class of systematically improvable interatomic potentials, Multiscale Model. Simul. **14**, 1153 (2016).
[45] G. C. Capitani, S. Di Pierro, and G. Tempesta, The 6H-SiC structure model: further refinement from SCXRD data from a terrestrial moissanite, Am. Mineral. **92**, 403 (2007).
[46] D. R. Lide (ed.), *CRC Handbook of Chemistry and Physics* (CRC Press, Boca Raton, FL, 2005).
[47] Y. S. Suh, S. P. Joshi, and K. T. Ramesh, An enhanced continuum model for size-dependent strengthening and failure of particle-reinforced composites, Acta Mater. **57**, 5848 (2009).
[48] A. G. Every and A. K. McCurdy, *Table 3. Cubic system. Elements, in: Landolt-Börnstein-Group III Condensed Matter Numerical Data and Functional Relationships in Science and Technology*, Vol. 29a (Springer, Berlin, 1992).
[49] T. Huber, H. P. Degischer, G. Lefranc, and T. Schmitt, Thermal expansion studies of aluminum-matrix composites with different reinforced architecture of SiC particles, Compos. Sci. Technol. **66**, 2206 (2006).
[50] W. Zheng, X. He, M. Wu, S. Ren, S. Cao, D. Guan, R. Liu, and X. Qu, Thermal expansion coefficient of diamond/SiC composites prepared by silicon vapor infiltration in vacuum, Vacuum **159**, 507 (2019).
[51] A. K. Collins, M. A. Pickering, and R. L. Taylor, Grain size dependence of the thermal conductivity of polycrystalline chemical vapor deposited β-SiC at low temperatures, J. Appl. Phys. **68**, 6510 (1990).
[52] D. T. Morelli, J. P. Heremans, C. P. Beetz, W. S. Yoo, and H. Matsunami, Phonon-electron scattering in single crystal silicon carbide, Appl. Phys. Lett. **63**, 3143 (1993).
[53] D. T. Morelli, J. P. Heremans, and G. A. Slack, Estimation of the isotope effect on the lattice thermal conductivity of group IV and group III-V semiconductors, Phys. Rev. B **66**, 195304 (2002).
[54] D. G. Cahill, S. K. Watson, and R. O. Pohl, Lower limit to the thermal conductivity of disordered crystals, Phys. Rev. B **46**, 6131 (1992).